Type of the Paper (Article)

Estimating Full Regional Skeletal Muscle Fibre Curvature from b-Mode Ultrasound Images Using Convolutional-Deconvolutional Neural Networks

Ryan Cunningham [1],*, María B Sánchez [1], Greg May [1] and Ian Loram [1],*

[1] School of Healthcare Science, Manchester Metropolitan University, Manchester, England, UK

* Correspondence: ryan.cunningham@mmu.ac.uk, i.loram@mmu.ac.uk

Abstract: Direct measurement of strain within muscle is important for understanding muscle function in health and disease. Current technology (kinematics, dynamometry, electromyography) provides limited ability to measure strain within muscle. Regional fiber orientation and length are related with active/passive strain within muscle. Currently, ultrasound imaging provides the only non-invasive means of observing regional fiber orientation within muscle during dynamic tasks. Previous attempts to automatically estimate fiber orientation from ultrasound are not adequate, often requiring manual region selection, feature engineering, providing low-resolution estimations (one angle per muscle), and deep muscles are often not attempted. Here, we propose deconvolutional neural networks (DCNN) for estimating fiber orientation at the pixel-level. Dynamic ultrasound images sequences of the calf muscles were acquired (25 Hz) from 8 healthy volunteers (4 male, ages: 25–36, median 30). A combination of expert annotation and interpolation/extrapolation provided labels of regional fiber orientation for each image. We then trained DCNNs both with and without dropout using leave one out cross-validation. Our results demonstrated robust estimation of regional fiber orientation with approximately 3° error, which was an improvement on previous methods. The methods presented here provide new potential to study muscle in disease and health.

Keywords: ultrasound; b-mode; skeletal muscle; fascicle orientation; pennation angle; fiber orientation; fiber tract; fascicle tract; convolutional neural network; deconvolutional neural network

1. Introduction

This paper presents a novel application of deconvolutional neural networks for estimating full regional skeletal muscle fiber orientation directly from standard frame rate (25Hz) b-mode ultrasound images. In recent years, ultrasound has become a valuable and ubiquitous clinical and research tool for understanding the changes which take place within muscle in ageing, disease, atrophy, and exercise. Ultrasound has been proposed [1] as a non-invasive alternative to intramuscular electromyography (iEMG) for measuring twitch frequency, useful for early the diagnosis of motor neuron disease (MND). Ultrasound has also recently demonstrated application to rehabilitative biofeedback [2]. Other computational techniques have been developed for muscle-ultrasound analysis which would allow estimation of changes in muscle length during contraction[3], and changes in fiber orientation and length [4]–[8]. Regional muscle fiber orientation (curvature) and length change when muscle is under active (generated internally through contraction) and/or passive strain (generated externally through joint movements or external pressure) [9], [10]. Muscle fiber orientation is one of the main identifying features of muscle state [11]. Below, we review the previous computational methods which attempt to automatically estimate fascicle orientation from ultrasound

42   images of skeletal muscle. We do not consider feature tracking based approaches [8], [12], since
43   within ultrasound feature tracking is an ill-posed problem, leading to tracking drift and feature
44   dropout due low signal to noise ration and out of plane feature motion [13].

45   Previous attempts to automatically estimate fiber orientation directly from b-mode ultrasound
46   images are inadequate, typically requiring manual region identification, *a priori* feature engineering,
47   presumptuous problem approach (e.g. fascicles and connective tissues appear as straight lines),
48   and/or typically providing low resolution estimates (i.e. one angle for an entire muscle region).
49   Further, to our knowledge, nobody has attempted the deep (more challenging) muscles. All previous
50   methods depend on some parameterization of features such as Gabor wavelets [4], [5], and/or edge
51   detectors and vessel enhancement filters [4]–[8], [14]–[16]. In all cases, parameters are empirically
52   chosen and/or are based on assumptions about how the descriptive features will present within an
53   image. In the studies we are aware of, parameters are chosen presumptuously or empirically rather
54   than tuned with a multiple-fold cross-validation set, and since the authors unanimously write that
55   results are sensitive to parameter changes, the assumption is that real world performance may not be
56   as optimistic as reported.

57   Zhou and colleagues [17] developed a method based on the Revoting Hough Transform (RVHT)
58   which provides an estimate of the overall fiber orientation in a single muscle, the gastrocnemius in
59   the calf. Based upon the incorrect assumption that the fiber paths are straight lines, they use the RVHT
60   to detect an empirically predetermined number of lines within a manually defined region of interest
61   and then take the median orientation of all detected lines as the overall orientation of the fibers. The
62   approach of Zhou and colleagues is fundamentally limited to detecting straight lines, whereas muscle
63   fibers do not always present that way. When observing muscle fibers using ultrasound, there are
64   many other features which can appear as straight lines (blood vessels, noise/dropout,
65   artefacts/reflections, skin/fat layers, connective tissues, etc…). These fundamental facts are a strong
66   limiting factor to the potential of methods such as the RVHT and the Radon Transform [7].

67   Rana and colleagues [5] introduced a method which potentially allowed estimation of local
68   orientation, although after suggesting this, the mean of local orientations is used to produce another
69   method which provides an estimate of the overall fiber orientation. Local orientations were identified
70   by convolving a bank of Gabor Wavelet filters with a processed version of the image. They compare
71   their proposed method with manual annotations from 10 experts and the Radon Transform, which
72   like the Hough Transform (or RVHT) is a method which can be used for detecting straight lines in
73   images. Both the Radon Transform and Wavelet methods require a preprocessing step described as
74   vessel enhancement filtering, which enhances anisotropic features within the image. The vessel
75   enhancement method is parametric, where parameters were chosen empirically with no cross-
76   validation or evaluation of results over varying parameters. Their results showed that the Radon
77   Transform was not significantly different to the expert annotations, whereas the Wavelet method was
78   significantly different. Other than significance values, the only accessible results they report are mean
79   differences (1.41°) between the Wavelet method and the expert annotations of real images, and mean
80   differences between both the Radon and Wavelet method applied to synthetic images with known
81   orientations (< 0.06°). Although the Wavelet method performed comparatively poorly, the authors
82   rightly suggest that this approach has potential to allow tracking of fiber paths throughout the
83   muscle, whereas Radon and Hough Transform methods do not.

84   Namburete and colleagues [6] expanded upon the methods of Rana and colleagues [5],
85   developing the hypothesis that regional fiber orientation can be tracked using local orientated Gabor
86   Wavelets and vessel enhancement filters, for the first time going beyond linear approximations to the
87   overall orientation. The proposed extension is to convolve the local orientations with a median filter,
88   which effectively smooths the local orientations. The fiber trajectories are then tracked between the
89   muscle boundaries on a continuous coordinate system with linear (following the dominant
90   orientation in a local 15 × 15-pixel region centered on the current fiber track) steps of 15 pixels. Finally,
91   curvature is quantified using the Frenet-Serret curvature formula [18]. Namburete's method differs
92   significantly from all preceding methods because it provides an estimation of local fiber orientation,
93   rather than a more global estimate. However, the authors do not provide an estimate of the error for
94   example when comparing to expert annotations; instead they evaluate errors on synthetic images
95   with known orientations, which are trivial. Further, they do not apply this method to the deeper
96   muscles, which are even more challenging.

97   Several important problems have been identified as unaddressed from a review of previous
98   methods for estimating full regional fiber orientation in multiple layers of muscle; most commonly,
99   the lack of error evaluation on real data, estimating overall fiber orientation and not local orientation,
100   limited application to superficial muscles only, and presumptuous justification for chosen
101   parameters. We propose to address these problems by introducing advanced machine learning
102   methods and cross-validation against expert annotation of real data. In recent years the popularity of
103   machine learning (in particular neural networks) has surged since a number of successive
104   algorithmic, methodological, and computational hardware developments were introduced [19]–[23].
105   The application of machine learning to estimating local fiber orientations has thus far not been
106   considered. In recent years, the development of deconvolutional neural networks (DCNN) allows
107   robust regression (heatmaps [24]–[26]) or classification (semantic segmentation [27]) of pixel level
108   labels in full resolution images, without any feature engineering or preprocessing (i.e. all parameters
109   are learned from data, and cross-validated against held-out validation and test sets). Therefore, we
110   expect DCNNs to perform well at predicting fiber orientation heat maps from ultrasound images of
111   muscle. For comparison we implement a version of the wavelet method described by Namburete,
112   and colleagues [6], since no data are presented on the accuracy of their method on real ultrasound
113   images.

114   **2. Materials and Methods**

115   *2.1. Deep Learning Software*

116   All neural network software was developed from scratch by the authors using C/C++ and
117   CUDA-C (Nvidia Corporation, Santa Clara, California). No libraries other than the standard CUDA
118   libraries (runtime version 8.0 cuda.h, cuda_runtime.h, curand.h, curand_kernel.h,
119   cuda_occupancy.h, and device_functions.h) and the C++ 11 standard library were used. All DCNNs
120   were trained on an Intel Xeon CPU E5-2697 v3 (2.60GHz), 64GB (2133 MHz), Nvidia with a TitanX
121   (Maxwell) GPU.

122   *2.2. Data Acquisition*

123   Ultrasound image data were recorded at 25Hz (AlokaSSD-5000 PHD, 7.5MHz) from the calf
124   muscles (medial gastrocnemius and soleus) of 8 healthy volunteers (4 male, ages: 25-36, median 30)

125 during dynamic maximum isometric voluntary contractions. Images represented a 6cm × 5cm
126 (horizontal × vertical axes) cross-section of the calf muscles. Volunteers lay prone on a physio bed
127 with their right ankle strapped to a immobilised pedal. Volunteers were asked to push their toes
128 down against the pedal as hard as they could. A dynamometer (Cybex) recorded the torque at 100Hz
129 at the ankle during the contraction. Matlab (Matlab, R2013a, The MathWorks Inc., Natick, MA) was
130 used to acquire ultrasound frames and a hardware trigger was used to initiate recording at the start
131 of each trial.

132 *2.3. Generating Ground Truth*

133   Following data collection, we extracted all frames beginning one frame before contraction
134 started, and ending with the frame when contraction peaked, where initial and peak contraction were
135 identified manually. This resulted in a total of 504 images containing spatiotemporal variations in
136 both fiber orientation and muscle thickness. Two experts were asked to manually identify fiber paths
137 in all muscles/compartments in all images by marking a series of multiple-point lines/curves
138 (typically 20-30 per muscle/compartment). The same experts were asked to identify the boundaries
139 of the medial gastrocnemius (superficial muscle) and the boundaries and internal compartments
140 (where visible) of the Soleus (deep muscle) by marking multiple-points lines/curves around the
141 boundaries and visible intramuscular compartments.

142   To create labels for each pixel, first a blank image (matrix of zeros with equal dimensions to the
143 ultrasound image) was created. Then, the angles along each of the annotated fiber lines were
144 calculated, and for each pixel under the lines the calculated angle was stored. The result was an image
145 of mostly zeroes and a few angled lines, where the value of the non-zero pixels represents the local
146 angle of the line intersecting each pixel. Then, within each muscle/compartment (defined by the
147 experts), nearest neighbor interpolation was used to fill the gaps between lines, followed by nearest
148 neighbor extrapolation to fill the muscle/compartment. Between muscles/compartments, nearest
149 neighbor interpolation was also used to fill the gaps. All other pixels (outside muscle, e.g. skin) were
150 set to zero. Following, additional data were created to introduce variation in the data/labels and help
151 prevent over-fitting, by randomly (uniform) rotating each image and corresponding labels/angles
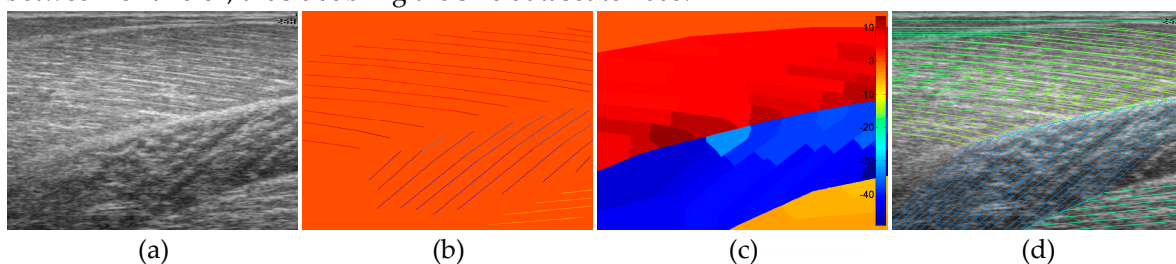152 between -5° and 5°, thus doubling the size dataset to 1008.

(a)   (b)   (c)   (d)

153 **Figure 1. Image annotation**. (a) shows the raw ultrasound image, (b) shows expert annotated line
154 traces of visible fibre paths, (c) shows nearest neighbor region filling of annotated fiber paths within
155 annotated muscles/compartments, (d) shows line traces over the filled regions. The colors in (b)-(d)
156 represent the local fibre orientation in degrees (see colour bar in (c)).

157 *2.4. Wavelet Filter Bank Method*

158   The wavelet method was implemented faithful to the original paper [6]. A bank of 180 Gabor
159 wavelet filters was generated spanning 0°-179° in 1° increments using,

160
$$g(x,y) = -e^{\left(\frac{(x-k-1)^2(y-k-1)^2}{-dk}\right)}\cos\left(\frac{2\pi\left((x-k-1)\cos(\alpha)-(y-k-1)\sin(\alpha)\right)}{f}\right),$$

161 where k is the kernel size (k = 20), d is a damping term (d = 51.243), α is the orientation, and f is the
162 spatial frequency (f = 7). Initially, all parameters were set as originally described in [6], and after a
163 first analysis, some parameters (f and k) were varied (f = 9, f = 11, f = 13, k = f*3-1) to give some scope
164 to the potential of this method on real data. Vessel enhancement was performed using a Matlab
165 version of the Frangi multiscale vessel enhancement filter [28] which can be found here [29].
166 Following [6], filtering was performed at 3 resolutions, 2, 3, and 4. Following a first analysis, a second
167 analysis was done at resolutions, 4, 6, and 8, for all variants of the Gabor wavelet filters described
168 above.

169   To analyse an image, the image was filtered with the vessel enhancement filter and then
170 convolved with the entire wavelet filter bank. At each spatial location in the image, we take the α
171 corresponding to the filter with the highest convolution in that location. The result is a map of local
172 orientations. Following [6], the image was then convolved with a 35 × 35 median filter resulting in
173 the final map of local fiber orientations.

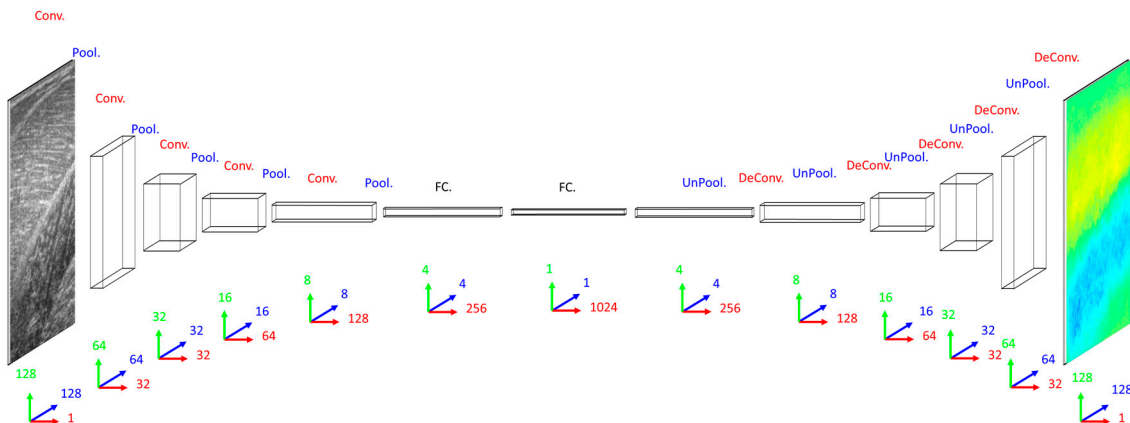174 *2.5. Deconvolution Neural Network Method*

175 **Figure 2. DCNN schematic**. On the far left the grayscale input image is connected to a series of
176 convolutional (Conv.) and max-pooling (Pool.) layers, followed by a series of fully connected (FC.)
177 layers, followed by a series of max-un-pooling (UnPool.) and deconvolutional (DeConv.). The green,
178 blue and red arrows and numbers represent the vertical and horizontal axes, and the number of filters
179 (or depth/color channels with respect to the input/output layers) respectively in each layer. This
180 network has 1,942,528 units (neurons), and 9,187,904 trainable weights/biases (synapses).

182   Our primary concern when deciding on a DCNN architecture (number of layer and units per
183 layer) was having a large enough model to learn the training set. Our secondary concern was training
184 time, since we planned to execute an 8-fold cross-validation. Addressing the latter concern, both
185 input images and labels were down-sampled (bilinear interpolation) to 128 × 128 pixels. Addressing
186 the former concern, the DCNN implemented 32 convolutional filters in the input layer, with 4
187 additional convolutional layers, the first of which had 32 filters and each of the following had double
188 the number of filters in the preceding convolutional layer. Between convolutional layers, the spatial
189 dimensions were down-sampled (max-pooling) by a factor of 2. A dense fully connected layer of 1024
190 nodes was fully connected to an initial up-sampling (2 × 2 max-un-pooling) layer, followed by a
191 deconvolution layer. An additional 4 up-sampling with deconvolutional layers following, completes

192   the network architecture, with the final layer being a full 128 × 128 resolution regression map. Every
193   layer consisted of rectified linear units (ReLU), with the exception of the final (output) layer, which
194   consisted of linear units. The DCNN was trained by minimizing mean square error (MSE) between
195   the labels and the output layer using online stochastic gradient descent (batch size of 1 sample).
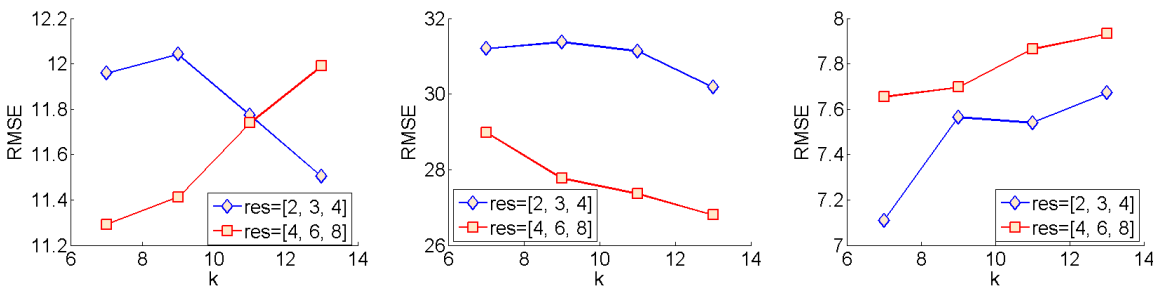
196   *2.6. DCNN Cross-Validation and Regularization*

197   To optimize and test generalization (estimated real-world performance), leave one person out
198   cross-validation was performed on 3 DCNNs with different dropout parameter settings (0%, 30%,
199   50%), where dropout was enabled in the fully connected layers only. A small amount of L2 weight
200   decay was used, $5e^{-4}$, to prevent the weights from growing too large and to help convergence. The
201   weights of the DCNNs were initialized using Xavier initialization [30]. To train the DCNNs we used
202   a learning rate of $5e^{2}$ and weight gradient momentum of $9.5e^{-1}$, for a maximum of 300 full batch
203   iterations (approx. 300,000 weight updates) using stochastic online gradient descent (minibatch=1).
204   All learning parameters were chosen empirically on a small fraction of the training data. The DCNNs
205   were trained 8 distinct times (one for each person), each time reinitializing the networks and leaving
206   a different person out for testing, and randomly splitting the remaining data (7 people) into validation
207   and training sets (10% and 90% respectively). Prior to training, each pixel of the input images was
208   normalized over the training set to zero mean and unit variance, and each pixel of the output images
209   was divided by a constant (45) so that most of the pixels (angles) fell between -1 and +1. Validation
210   and test errors were observed periodically, and the test error observed at the lowest validation error
211   (early stopping method) gave results for the validation set and the test set (estimated real-world
212   generalization error) for the held-out person. Test results for all held-out participants were combined
213   to reveal the performance of the optimal DCNN.

3. Results

215   Following model optimization of the wavelet and DCNN methods, both methods were
216   compared against the ground truth labels using a range of error measures, thus making the work
217   accessible and comparable to others. In sections 3.1 and 3.2 results are presented respectively for the
218   wavelet method and the DCNN method. With respect to data ranges, within the GM muscle, the
219   maximum range of angles within a single muscle region was 34.84°, whereas the maximum range of
220   angles over all participants was 76.58°. Within the Sol muscle (compartment 1), the maximum range
221   of angles within a single muscle region was 35.02°, whereas the maximum range of angles over all
222   participants was 64.92°. Within the Sol muscle (compartment 2), the maximum range of angles within
223   a single muscle region was 65.15°, whereas the maximum range of angles over all participants was
224   79.05°.

225   *3.1. Wavelet Method*

GM   Sol (1st compartment)   Sol (2nd compartment)

226 **Figure 3. Wavelet parameter tuning**. This graphic depicts how the error changes with respect to the
227 parameters of the Frangi filter (res), and the Gabor wavelet filters (k).
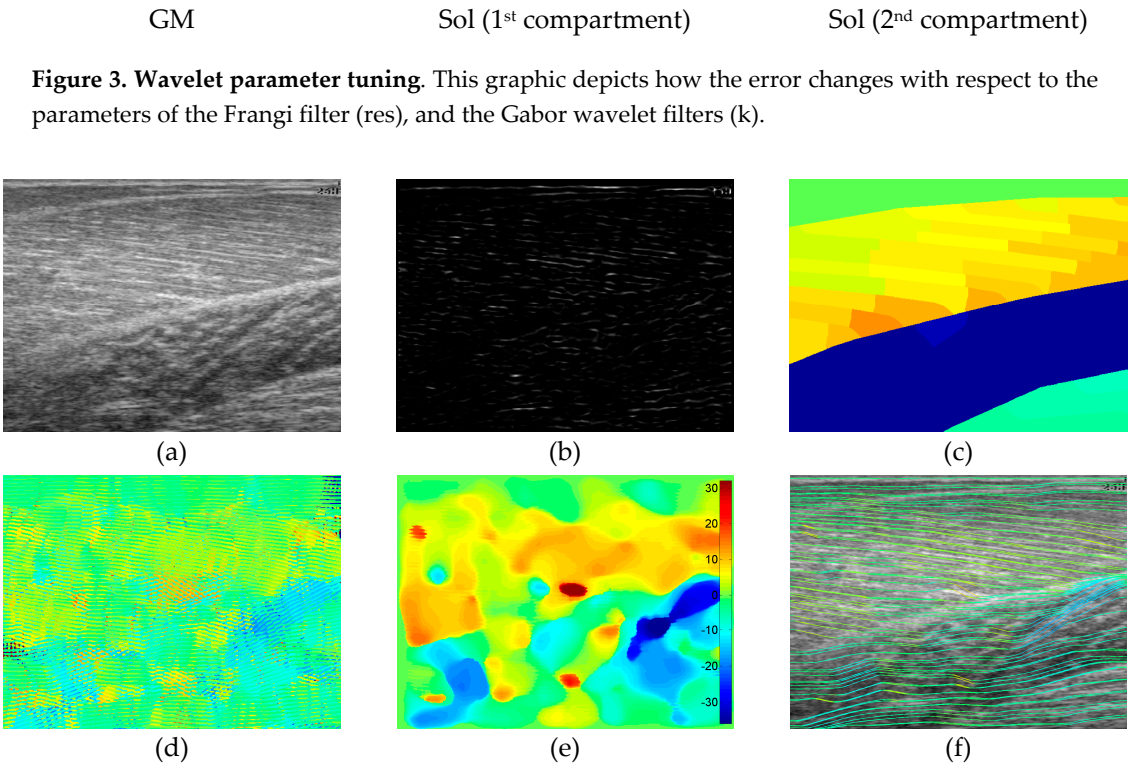
228

(a)   (b)   (c)

(d)   (e)   (f)

229 **Figure 4. Representative wavelet visual result**. (a) shows the raw image, (b) shows the vessel-
230 enhanced image, (c) shows the ground truth, (d) shows the result of Gabor wavelet convolution with
231 (b), (e) shows the result of a (35 × 35) median filter applied to (d), (f) shows line traces of (e). It is clear,
232 when comparing (e) to (c), that the heatmaps partial match within the GM region, but almost not at
233 all in the Sol region. The line trace visually confirms that the fibre traces are roughly aligned with the
234 visible fibres in the raw image in the GM muscle, and the second compartment of the Sol muscle only.

235

236 The wavelet method was evaluated using the optimal parameters (within the range of
237 parameters investigated) for each muscle/compartment, separately. To find the optimal parameters
238 within each muscle, the local orientation over each pixel identified by the wavelet method was
239 compared to each pixel of the ground truth by root mean square error (RMSE) (see fig. 3). Within the
240 parameters we investigated, for the GM muscle, smaller wavelet filters resulted in smaller RMSE for
241 the higher-resolution Frangi filter (res= [4, 6, 8]), conversely larger wavelet filters results in smaller
242 RMSE for the lower-resolution Frangi filter. Within the parameters we investigated, the first
243 compartment of the Sol muscle yields best results with the higher-resolution Frangi filter and larger
244 wavelet filters. Conversely, within the parameters we investigated, the second compartment of the
245 Sol muscle yields best results for smaller wavelet filters and lower-resolution Frangi filter. The
246 models with the lowest RMSE were compared to ground truth using mean difference (MD) and mean
247 absolute error (MAE), to be compared with the DCNN method (section 3.2).
248 For the optimal models within each muscle/compartment, the deviations of predicted local fibre
249 orientations from ground truth were much too high to be useful in any real context, particularly in
250 the Sol (compartment 1) muscle, which reports an optimal RMSE of over 26° (see fig. 3). Discrepancies
251 were much lower in the GM and Sol (compartment 2) muscles at 11.3° and 7.1°, respectively. Visual
252 comparisons were also made by comparing the wavelet analysis, presented as a heat-map, to the
253 ground truth, also presented as a heat-map (see fig. 4). Visual comparison revealed quite sporadic
254 agreement between wavelet predictions and ground truth. Visual comparison also revealed that any
255 agreement between wavelet predictions and ground truth was not only heavily dependent on the

256 presence of well-defined muscle fibre tracts, but also on the ability of the Frangi filter to extract those
257 features.
258   Application of the wavelet method was computationally expensive using the Matlab framework,
259 with full regional analysis (whole image including all muscles) taking between one and two hours to
260 process all 504 images for a single set of parameters. We note that this can be significantly improved
261 upon with the use of graphics processing units (GPUs) and/or a full compiled language (such as
262 C/C++).

263 *3.2. DCNN Method*

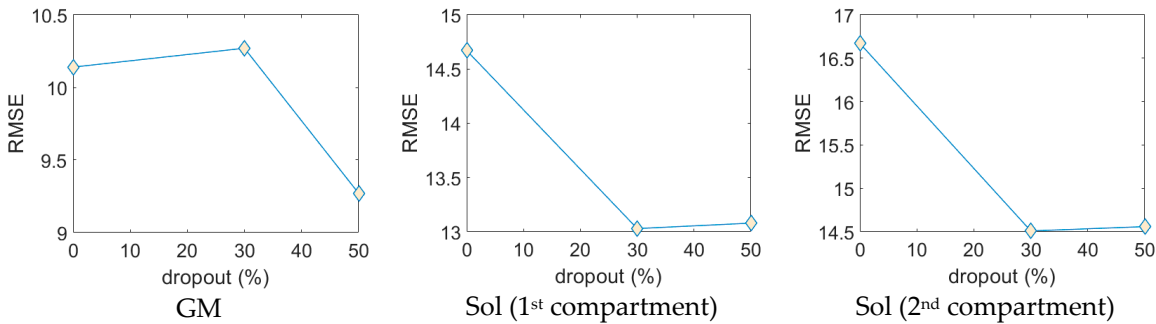GM   Sol (1st compartment)   Sol (2nd compartment)

264 **Figure 5. DCNN regularization**. This graphic depicts how the error changes with respect to the
265   percentage of dropout enabled in the fully connected layers of the DCNN. These results show that
266   dropout improved lowered RMSE, with 50% dropout being most effective, and therefore revealing
267   the optimal model.

268

269   The DCNN method was evaluated using the optimal models as identified by cross-validation
270 (see sec. 2.6) and regularization using dropout (see fig. 5). Following, the output heat-map from the
271 optimal DCNN for all 504 images were compared to the ground truth using mean difference (MD)
272 and mean absolute error (MAE), to be compared with the wavelet method (see sec. 3.1). Visual
273 comparisons were also made by comparing the DCNN predictions, presented as a heat-map, to the
274 ground truth, also presented as a heat-map (see fig. 5). The most immediate result of visual
275 comparisons was the ability of the DCNN to 'color-code' the correct regions; the GM and Sol
276 (compartment 1) muscles typically present with opposing fibre orientations, with negative angles in
277 the Sol muscle and positive angles in the GM muscle. In almost all images the DCNN was able to
278 identify the Sol and GM muscles simply by predicting negative and positive angles respectively for
279 each compartment. Furthermore, this was broadly true for entire muscle regions, even where there
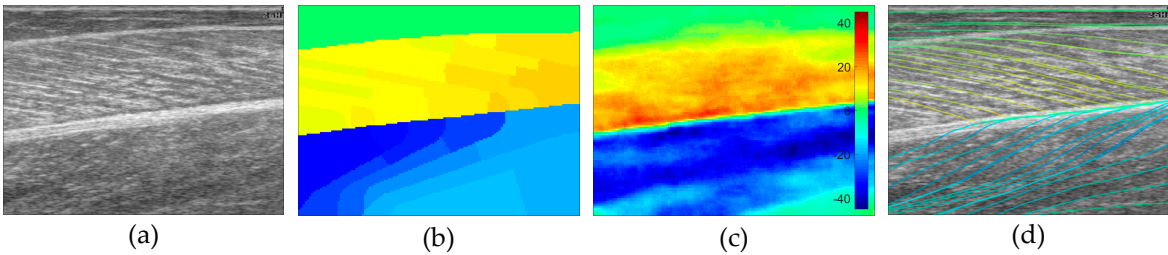280 were no visually identifiable fibre tracts (see fig. 5).

281

(a)   (b)   (c)   (d)

282 **Figure 5. Representative DCNN visual result**. (a) shows the raw ultrasound image, (b) shows the
283   ground truth, (c) shows the raw output from the DCNN, (d) shows line traces of (c). Careful
284   observation of (c) reveals that the DCNN has predicted a bifurcation in the deep part of the Sol muscle

285 (lower right), which disagrees with the expert in (b). Now look at the lower right portion of (a) and
286 see that this prediction is entirely plausible, as confirmed by (d) which shows line traces following
287 the visible fiber paths.

288

289 **Table 1.** Table of results per muscle/compartment. This table shows results computed by comparing
290 predictions of each method, over all pixels (128 × 128 = 16384), to the ground truth.

Muscle/ Compartment	Error Measure	Namburete, *et al* [6]	Proposed (DCNN)
GM	MD [1]	7.57° ± 8.37°	3.09° ± 8.74°
	MAE [2]	8.23° ± 7.72°	6.24° ± 6.85°
	RMSE [3]	11.29°	9.27°
Sol (1st Compartment)	MD [1]	-22.84° ± 14.01°	-4.99° ± 12.09°
	MAE [2]	23.09° ± 13.61°	10.64° ± 7.61°
	RMSE [3]	26.80°	13.08°
Sol (2nd Compartment)	MD [1]	1.61° ± 6.92°	10.64° ± 9.93°
	MAE [2]	5.03° ± 5.01°	12.25° ± 7.86°
	RMSE [3]	7.11°	14.56°

291 [1] mean difference. [2] mean absolute error. [3] root mean square error.

4. Discussion

293 In this paper we reviewed the state of the art computational methods for estimating regional
294 fibre orientation from ultrasound images of skeletal muscle. We found that the previous approaches
295 were fundamentally lacking in their comparison to real ultrasound data, thus rendering them
296 incomparable unless implemented. We also found that previous methods were targeted at estimating
297 global/overall muscle fibre orientation by using some line detection technique such as the Hough or
298 Radon transform [5], [7], [14], [17]. Fibres are known to curve within a muscle, and here we have also
299 provided data in support of this, based on expert identification of fibre tracts within 3
300 muscles/compartments over 8 people, which show how fibre orientation is different within a
301 muscle/compartment (see paragraph 1 of Results section).
302 In review of previous methods we found an approach which demonstrated potential to provide
303 estimates of local orientation [5], [6]. The authors did not present any comparable data to assess the
304 performance of this method on real ultrasound data, only reporting that there were significant
305 differences between their method and expert annotations of fibre orientation in real ultrasound
306 images. The authors also highlight weaknesses in their approach such as the need for manual region
307 identification, where the region selected should contain visibly well-defined fibre tracts. We
308 recognized the potential for this method to fail in the presence of noise, artefacts, other quasi-line
309 structures (blood vessels, connective tissues, etc.), and other muscles where fibres do not present as
310 clearly, such as the deep muscles.
311 We proposed the application of a deep learning method known as deconvolutional neural
312 networks (DCNN). We identified that such a method is capable of robust regression (heatmaps [24]–
313 [26]) or classification (semantic segmentation [27]) of pixel level labels in full resolution images. The
314 advantage of a deep learning approach is that the model can learn to identify fibres in well-defined
315 regions, interpolate between well-defined regions and extrapolate from regions to fill the
316 muscle/compartment with predictions of local fibre orientation. Deep learning models can also learn
317 to ignore regions with spurious (non-fibrous) features. After training 3 DCNNs with different levels
318 of dropout enabled, using 8-fold cross-validation and early stopping using a validation set, we
319 compared the results to the wavelet method applied to the same data. Results were compared within
320 specific muscle regions (identified by two experts) since large variations were expected due to the
321 challenging textural appearance of the deep muscles (Sol). Results revealed that both methods
322 showed large deviations from the ground truth, however the DCNN method gave much more
323 accurate predictions for the superficial and deep muscles (first compartment) than the wavelet

324 method. Those predictions were also much more consistent as identified by standard deviations of
325 the error metrics (see table. 1). Our results showed that dropout applied to fully connected layers,
326 improved overall performance of the DCNN, and we suggest that further improvement is possible
327 with additional tuning of the dropout parameter, or even the configuration of the network
328 architecture, and certainly with additional data. In contrast, although figure 3 indicates that there is
329 scope to tune the wavelet method, it is much harder to do so in such a way which generalizes and
330 deals with all of the problems we identified as well as the original authors (image artefacts, spurious
331 fibre features, noise, reflections, etc.).

5. Conclusions

333 In this paper have we provided the first comprehensive analysis of an existing and a novel
334 computational method for estimating full regional fibre orientation from ultrasound images of
335 human skeletal muscle. We have proposed a novel application of deep learning to a long-standing
336 and challenging problem, and demonstrated state of the art results. We present analyses in a form
337 which is comparable to any future developments, and we also publish our ultrasound and ground
338 truth data to support this end. The application of DCNNs to this problem has opened up new
339 potential to hi-resolution analysis of skeletal muscle, from prediction of motion maps to segmentation
340 of muscles and other structures of interest. This paper provides further evidence that deep learning
341 methods can surpass state of the art performance, even when there is not an abundance of labeled
342 data available. With additional data we propose that this project could easily be extended
343 successfully, and this preliminary muscle analysis step could very likely form part of a skeletal
344 muscle analysis system which accurately predicts the passive and active muscle forces non-invasively
345 directly from single ultrasound images and sequences. Such a contribution could enable early
346 diagnoses of diseases such as MND, and would enable personalized musculoskeletal medical
347 diagnosis, monitoring, treatment targeting, and care.

350 **Author Contributions:** Loram and Cunningham conceived the work. Loram, Cunningham and May designed
351 and performed the data acquisition experiment. Cunningham and Sánchez annotated muscle boundaries and
352 muscle fibre traces, providing ground truth for all images. Cunningham wrote the paper. All authors revised
353 versions of the paper. Cunningham wrote the wavelet analysis software in Matlab and performed the wavelet
354 analysis. Cunningham wrote the deep learning software in C++/Cuda-C and performed the deep learning
355 analysis. Loram was the supervisor of this work.

356 **Conflicts of Interest:** The authors declare no conflict of interest.

References

358 [1] P. J. Harding, I. D. Loram, N. Combes, and E. F. Hodson-Tole, "Ultrasound-Based Detection of
359 Fasciculations in Healthy and Diseased Muscles," *IEEE Trans. Biomed. Eng.*, vol. 63, no. 3, pp. 512–518,
360 2016.

361 [2] I. D. Loram, B. Bate, P. Harding, R. Cunningham, and A. Loram, "Proactive Selective Inhibition Targeted
362 at the Neck Muscles: This Proximal Constraint Facilitates Learning and Regulates Global Control," *IEEE*
363 *Trans. Neural Syst. Rehabil. Eng.*, vol. 25, no. 4, pp. 357–369, 2017.

364 [3] I. Loram, C. Maganaris, and M. Lakie, "Use of ultrasound to make noninvasive in vivo measurement of
365 continuous changes in human muscle contractile length," *J. Appl. Physiol.*, pp. 1311–1323, 2006.

366 [4] G. Q. Zhou, P. Chan, and Y. P. Zheng, "Automatic measurement of pennation angle and fascicle length
367 of gastrocnemius muscles using real-time ultrasound imaging," *Ultrasonics*, vol. 57, no. C, pp. 72–83,
368 2015.

369 [5] M. Rana, G. Hamarneh, and J. M. Wakeling, "Automated tracking of muscle fascicle orientation in B-
370 mode ultrasound images," *J. Biomech.*, vol. 42, no. 13, pp. 2068–2073, 2009.

[6]   A. I. L. Namburete, M. Rana, and J. M. Wakeling, "Computational methods for quantifying in vivo muscle fascicle curvature from ultrasound images," *J. Biomech.*, vol. 44, no. 14, pp. 2538–2543, 2011.

[7]   X. Chen, Q. Li, S. Qi, H. Zhang, S. Chen, and T. Wang, "Continuous fascicle orientation measurement of medial gastrocnemius muscle in ultrasonography using frequency domain Radon transform," *Biomed. Signal Process. Control*, vol. 20, pp. 117–124, Jul. 2015.

[8]   J. Darby, B. Li, N. Costen, I. Loram, and E. Hodson-Tole, "Estimating skeletal muscle fascicle curvature from B-mode ultrasound image sequences," *IEEE Trans. Biomed. Eng.*, vol. 60, no. 7, pp. 1935–1945, 2013.

[9]   R. D. Herbert, S. C. Gandevia, and R. D. Herbert, "Changes in pennation with joint angle and muscle torque: in vivo measurements in human brachialis muscle," *J. Physiol.*, vol. 484, no. Pt2, pp. 523–532, 1995.

[10]   M. V Narici, T. Binzoni, E. Hiltbrand, J. Fasel, F. Terrier, and P. Cerretelli, "In vivo human gastrocnemius architecture with changing joint angle at rest and during graded isometric contraction," *J. Physiol.*, vol. 496, no. 1, pp. 287–297, 1996.

[11]   R. L. Lieber, J. Fridé N, and J. Fridén, "Functional and Clinical Significance of Skeletal Muscle Architecture," *Muscle Nerve*, vol. 23, no. November, pp. 1647–1666, 2000.

[12]   J. Darby, E. F. Hodson-Tole, N. Costen, and I. D. Loram, "Automated regional analysis of B-mode ultrasound images of skeletal muscle movement." *J. Appl. Physiol.*, vol. 112, no. 2, pp. 313–327, 2012.

[13]   F. Yeung, S. F. Levinson, and K. J. Parker, "Multilevel and Motion Model-Based Ultrasonic Speckle Tracking Algorithms," *Ultrasound Med. Biol.*, vol. 24, no. 3, pp. 427–441, Mar. 1998.

[14]   Y. Zhou, J.-Z. Li, G. Zhou, and Y.-P. Zheng, "Dynamic measurement of pennation angle of gastrocnemius muscles during contractions based on ultrasound imaging," *Biomed. Eng. Online*, vol. 11, no. 1, p. 63, 2012.

[15]   G. Q. Zhou and Y. P. Zheng, "Automatic Fascicle Length Estimation on Muscle Ultrasound Images With an Orientation-Sensitive Segmentation," *IEEE Trans. Biomed. Eng.*, vol. 62, no. 12, pp. 2828–2836, 2015.

[16]   F. Chen, "Hand gesture recognition using a real-time tracking method and hidden Markov models," *Image Vis. Comput.*, vol. 21, no. 8, pp. 745–758, 2003.

[17]   Y. Zhou and Y. P. Zheng, "Estimation of Muscle Fiber Orientation in Ultrasound Images Using Revoting Hough Transform (RVHT)," *Ultrasound Med. Biol.*, vol. 34, no. 9, pp. 1474–1481, Sep. 2008.

[18]   H. Stark and N. Schilling, "A novel method of studying fascicle architecture in relaxed and contracted muscles," *J. Biomech.*, vol. 43, no. 15, pp. 2897–2903, 2010.

[19]   A. Krizhevsky, I. Sutskever, and G. E. Hinton, "ImageNet Classification with Deep Convolutional Neural Networks," *Adv. Neural Inf. Process. Syst. 25*, pp. 1–9, 2012.

[20]   K. He, X. Zhang, S. Ren, and J. Sun, "Deep Residual Learning for Image Recognition," *Arxiv.Org*, vol. 7, no. 3, pp. 171–180, 2015.

[21]   G. Hinton, "Dropout : A Simple Way to Prevent Neural Networks from Overfitting," vol. 15, pp. 1929–1958, 2014.

[22]   V. Nair and G. E. Hinton, "Rectified Linear Units Improve Restricted Boltzmann Machines," *Proc. 27th Int. Conf. Mach. Learn.*, no. 3, pp. 807–814, 2010.

[23]   L. D. Le Cun Jackel, B. Boser, J. S. Denker, D. Henderson, R. E. Howard, W. Hubbard, B. Le Cun, J. Denker, and D. Henderson, "Handwritten Digit Recognition with a Back-Propagation Network," *Adv. Neural Inf. Process. Syst.*, pp. 396–404, 1990.

[24]   T. Pfister, J. Charles, and A. Zisserman, "Flowing convnets for human pose estimation in videos," in *Proceedings of the IEEE International Conference on Computer Vision*, 2015, vol. 2015 Inter, pp. 1913–1921.

414   [25]   P. Fischer, A. Dosovitskiy, E. Ilg, ..., and T. Brox, "FlowNet: Learning Optical Flow with Convolutional
415   Networks," *Iccv*, p. 8, 2015.

416   [26]   C. Payer, D. Štern, H. Bischof, and M. Urschler, "Regressing heatmaps for multiple landmark localization
417   using CNNs," in *Lecture Notes in Computer Science (including subseries Lecture Notes in Artificial Intelligence
418   and Lecture Notes in Bioinformatics)*, 2016, vol. 9901 LNCS, pp. 230–238.

419   [27]   H. Noh, S. Hong, and B. Han, "Learning deconvolution network for semantic segmentation," in
420   *Proceedings of the IEEE International Conference on Computer Vision*, 2016, vol. 11–18–Dece, pp. 1520–1528.

421   [28]   A. F. Frangi, W. J. Niessen, K. L. Vincken, and M. a Viergever, "Multiscale vessel enhancement filtering,"
422   *Medial Image Comput. Comput. Invervention - MICCAI'98. Lect. Notes Comput. Sci. vol 1496*, vol. 1496, pp.
423   130–137, 1998.

424   [29]   D.-J. Kroon, "Hessian based Frangi Vesselness filter," *MATLAB Central/File Exchange*, 2010. [Online].
425   Available: https://uk.mathworks.com/matlabcentral/fileexchange/24409-hessian-based-frangi-vesselness-
426   filter. [Accessed: 01-Nov-2017].

427   [30]   X. Glorot and Y. Bengio, "Understanding the difficulty of training deep feedforward neural networks,"
428   *Proc. 13th Int. Conf. Artif. Intell. Stat.*, vol. 9, pp. 249–256, 2010.